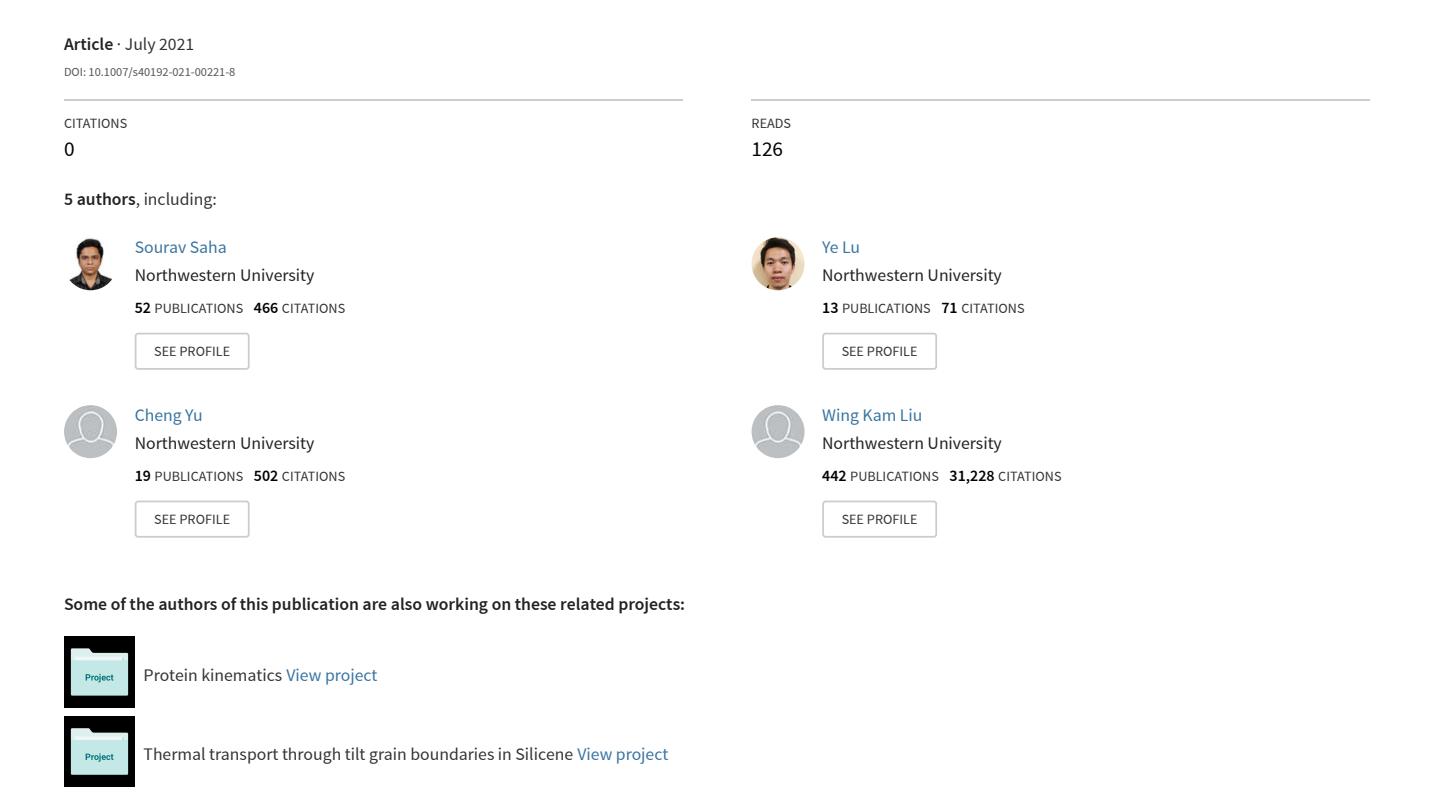
Macroscale Property Prediction for Additively Manufactured IN625 from Microstructure Through Advanced Homogenization



Macroscale Property Prediction for Additively Manufactured IN625 from Microstructure through Advanced Homogenization

Sourav Saha · Orion L. Kafka · Ye Lu · Cheng Yu · Wing Kam Liu*

Received: date / Accepted: date

Abstract Design of additively manufactured metallic parts requires computational models that can predict the mechanical response of the parts considering the microstructural, manufacturing, and operating conditions. This article documents our response to Air Force Research Laboratory (AFRL) Additive Manufacturing Modeling Challenge 3, which asks the participants to predict the mechanical response of tensile coupons of IN625 as function of microstructure and manufacturing conditions. A representative volume element (RVE) approach was coupled with a crystal plasticity material model, solved within the Fast Fourier Transformation (FFT) framework for mechanics, to address the challenge. During the competition, material model calibration proved to be a challenge, prompting the introduction in this manuscript of an advanced material model identification method using proper generalized decomposition (PGD). Finally, a mechanistic reduced order method called Self-consistent Clustering Analysis (SCA) is shown as a possible alternative to the FFT method for solving these problems. Apart from presenting the response analysis, some physical interpretation and assumptions associated with the modeling are discussed.

Sourav Saha

Theoretical and Applied Mechanics, Northwestern University, Evanston, Illinois, USA E-mail: SouravSaha2023@u.northwestern.edu

Ye Lu

Mechanical Engineering, Northwestern University, Evanston, Illinois, USA E-mail: ye.lu@northwestern.edu

Orion L. Kafka

National Institute of Standards and Technology (NIST), Materials Measurement Laboratory, Applied Chemicals and Materials Division, Boulder, CO, USA

Wing Kam Liu

Mechanical Engineering, Northwestern University, Evanston, Illinois, USA E-mail: w-liu@northwestern.edu, Corresponding author

 $^{^{}st}$ Corresponding author

Keywords Additive Manufacturing \cdot IN625 \cdot Proper Generalized Decomposition \cdot Self-consistent Clustering Analysis \cdot Homogenization

1 Introduction

Additive manufacturing (AM) technologies provide significant advantages not only in terms of production of parts with complex geometry, but also the flexibility to tune the material properties through optimized process control. However, a major drawback in establishing a process-structure-property relationship in AM is the spatial heterogeneity of microstructure in AM parts resulting from various factors including manufacturing conditions, build angle, geometry, and post-manufacturing treatment. Such variations are hard to incorporate into computational design consideration. To achieve the latter, the process-structure-property relationships can be determined using computational simulations [1,2,3,4]. For example, the build angle, conditions, geometry, and manufacturing conditions can be modeled by computational fluid dynamics, resulting microstructures by cellular automaton, and finally the resulting mechanical properties by computational solid mechanics models [1]. Air Force Research Laboratory Challenge 3 is designed to test models that can predict the mechanical response of AM built IN625 based on the characterized microstructure and calibration data. This work presents a structureproperties modeling methodology, followed by our answers to the AFRL Challenge 3 problems, including a discussion of our efforts to improve the material model calibration and data-driven homogenization after the competition was completed.

Use of computational techniques to model the effect of different factors such as precipitates [5], defects [6], texture [7], and temperature [2] has been seen for last few years owing to the popularity and perceived potential of AM technology such as powder bed fusion. Although some studies are multiscale, in order to incorporate the microstructural effects explicitly, materials design engineers often opt to use mechanistic or empirical relationships to connect the structure to property [8]. Two multiscale homogenization methods are demonstrated in the following sections to answer the challenge problems.

Microstructure-based mechanical response prediction of metals have been done with direct numerical methods such as the finite element method and the Fast Fourier transform [9] combined with crystal plasticity material models, also known as the crystal plasticity finite element method (CPFEM) [10] and crystal plasticity Fast Fourier transform (CPFFT) [11]. However, the tremendous computational cost of these methods, e.g. hours or days of computational time on a supercomputer with 1000 + cores [12], prevents their practical applicability to the modeling of large parts with spatial microstructure variation, as is the case in AM. Multiscale methods such as FE-FE (or FE²) [13] and FE-FFT [14] are proposed to alleviate this issue by scale separation and concurrent coupling between macroscale integration points and the corresponding microstructure volume elements (MVEs), but are still too expensive to

be used to model large complex parts. In this regard, a myriad of reducedorder methods have been developed for efficient multiscale simulations, see a recent review in [15]. Recently, the mechanistic data-driven method called self-consistent clustering analysis (SCA) proposed by Liu et al. [16] has been shown to maintain accuracy and efficiency for multiscale modeling of polycrystals [17,18]. Considering the nature of the challenge to be solved and the time constraints, we opted to use representative volume element (RVE) approach to predict the mechanical properties of the material [19].

Crystal plasticity models are used to predict the mechanical properties of additively manufactured alloys when considering the microstructural features [20]. Depending on the exact level of the physics to be modeled there are many the choices of crystal plasticity formulation [21]. Irrespective of the scenario, certain material parameters such shear yield stress, dynamic hardening, and recovery factor in these models have to be calibrated before they can be used to explore a larger material design space. Material parameters calibration is an optimization process, which often requires iteratively evaluating the cost function (e.g. the difference between predictions and testing data, in the present work this could be the stress at a given strain value) and possibly its gradients for different values of the parameter set of interest. The specific requirements of the cost function depend upon context and can be written to include comparison of everything from simple one-dimensional data-points to full field quantities although these examples should not be considered limitations. The usual way of calibrating the material parameters is using multi-objective genetic optimization [22, 23] coupled with full-field solution of the equations with either FEM or FFT. However, it is time consuming and thus a surrogate model is a better option to replace the full-field solution in the calibration process. For this challenge, a proper generalized decomposition (PGD) method [24,25] was combined with an adaptive sampling method to build a surrogate model capable of fast material parameter calibration when used with an optimization algorithm. This PGD-based approach is shown to be efficient and can be applied to high dimensionality problems. Other surrogate modeling approaches usually suffer from the curse of dimensionality.

This work is organized as follows: Section 2 summarizes the AFRL Challenge 3 problem, including the material of interest, the characterization, calibration data, and requested predictions. Section 3 presents the material modeling framework used. The PGD-based calibration method is given in Section 4.2. Results and discussion are provided in Section 5, future outlook is provided in 6 and the concluding remarks in Section 7.

2 Problem Statement

The AFRL Challenge 3 statement requests that participants predict various facets of tensile stress-strain curves under a range of different conditions. The goal is to assess the ability of the modelling community to make continuum-level predictions of common tensile mechanical properties for material pro-

duced with AM under a range of mechanical and material conditions. To enable the predictions, participates were asked use certain chemical, material, and mechanical information made available by the AFRL in the initial challenge statement.

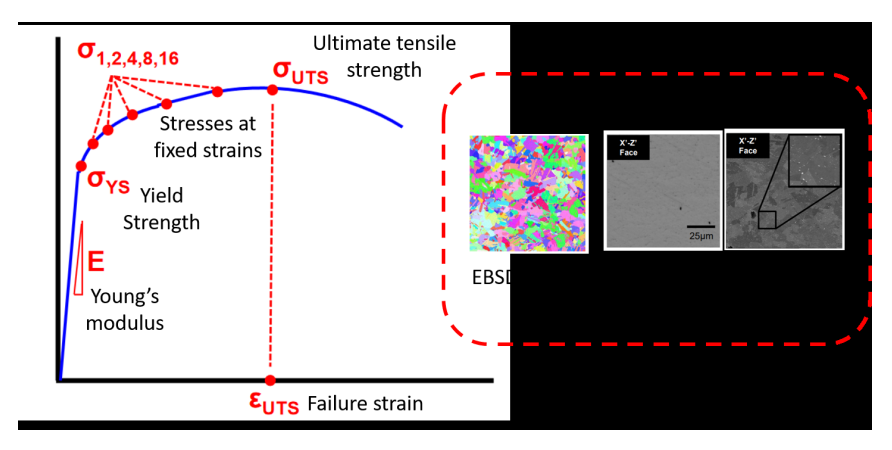


Fig. 1 A schematic diagram showing the overall desirable for AFRL Challenge 3. The participants had to predict the part-scale mechanical properties as shown in the figure, where the σ subscripts represent the strain levels, in %, requested. The provided information included EBSD characterization, optical microscopy, and backscattered electron images. The points 1, 2, 4, 8, and 16 mean stresses corresponding to 1%, 2%, 4%, 8%, and 16% strains.

2.1 Data provided

A full description of the Challenge, including all data provided, is supplied in an accompanying article in this Topical Collection and the challenge website [26].

The following sections will outline the information required for the subsequent modeling sections.

2.1.1 Material

Gas atomized IN625 stock material, with pre-build chemical composition measured by the material supplier listed in Tab. 1. Post-build 2D powder size analysis using laser particle size analysis (but not conducted by the AFRL) indicated sizes ranging from about 3 μ m to 65 μ m, with dual peaks at about 6.5 μ m and 22 μ m [26]. The specimens were produced on an laser powder bed fusion machine, EOS M280¹ using nominal build parameters. All material was

¹ Certain commercial software, equipment, instruments or materials are identified in this paper to adequately specify the experimental procedure. Such identification is not intended to imply recommendation or endorsement by the National Institute of Standards and Tech-

С	Si	Mn	P	S	Cr	Ni	Mo	CbTa	
0.3	< 0.01	< 0.01	< 0.004	0.002	21.20	Bal	8.91	3.56	
0.01	0.05	< 0.01	< 0.001	< 0.01	21.69	Bal	9.06	3.75	
Ti	Al	В	Со	Cu	Fe	N	О	Та	Mg
0.01	0.05	0.001	< 0.01	0.01	3.09	0.008	0.015	< 0.01	< 0.001
0.02	0.04	0.001	< 0.01	0.01	2.12	0.005	0.035	< 0.02	< 0.001

Table 1 Powder chemistry data as provided by the powder supplier prior to the build, in weight faction, reproduced from a PDF available at the AFRL Modeling Challenge Series website [26]

stress relieved (SR), while some specimens were also hot isostatically pressed (HIPped) and heat treated (HT). Calibration specimens were surface finished with low-stress grinding, while predictions were requested under both low-stress ground and as-built surface conditions. As-built surface roughness was reported as mean absolute distance from centerline (R_a), measured after image segmentation of representative cross-sections. No further raw material, processing, post-processing, specimen machining, or specimen handling data was provided beyond what is summarized here and provided in the data for participants, available at the time of publishing at [26].

2.1.2 Characterization

Microstructural characterization in the form of optical microscopy, electron backscatter diffraction (EBSD), and backscatter electron microscopy was reported for the calibration specimens, spanning the SR only and SR plus HIP plus HT for two or three orthogonal faces. Further, pole figures and descriptive statistics for grains, voids, and precipitates was provided. Equivalent microstructural characterization was provided for each prediction case requested. For as-built specimens, surface roughness, summarized as an R_a number, was also reported. EBSD characterization also indicated that as-built specimens had a layered grain size structure, with finer more equiaxed grain structure near the surfaces and larger columnar structure near the center. This grain structure was observed in the EBSD maps, but not differentiated in the summary statistics provided. Table 2 summarizes the characterization data on microstructure and mechanical properties considered in this challenge.

2.2 Calibration Data

Calibration test specimens were printed with the build direction aligned with the tensile loading axis, defined as the zero degree orientation. The ASTM E8

nology, nor is it intended to imply that the equipment or materials identified are necessarily the best available for the purpose.

specimens [27] of 15 mm diameter were machined from printed cylinders and low-stress surface-ground. Stress-strain curves for SR-only and SR+HIP+HT at each of 75 °F (as reported, approximately 23.9 °C) (room temperature, RT) and 1600 °F (as reported, approximately 871 °C) (elevated temperature, ET) were reported, in addition to summary statistics extracted from these curves, specifically Elastic Modulus, 0.2 % Offset Yield Strength, Stress at 1 %, 2 %, 4 %, 8 %, 16 % Engineering Strain, Ultimate Tensile Strength, and Uniform Elongation. Detailed material characterization was supplied for all the calibration cylinders.

2.3 Requested predictions

Figure 1 shows the key takeaways from the challenge problem. The nine different values describing the stress-strain curve given for the calibration data were requested for each of four different prediction conditions. The conditions were as-built, surface ground, SR-only, SR+HIP+HT, RT, ET, 0° build angle, 40° build angle, 1 mm thick specimens, and 5 mm thick specimens. Not all permutations of these were requested, and for ET specimens 16 % strain and Uniform Elongation results were not required.

The AFRL tested all the relevant specimens and recorded results with which to compare to the challenge predictions. Specific geometries of the tensile bars for calibration and geometries used to create the challenge data were provided to participants. Test equipment and conditions were nominally industry standard, although not specified in detail to the participants. Table 3 is a summary of the levels of each testing condition parameter covered for both calibration and modeling validation. See the challenge website, and associated data repositories and descriptions, for more details [26].

 ${\bf Table~2~Summary~of~microstructure~and~mechanical~properties~data}$

Microstructure	Data type	Mechanical properties	Data type	
Grains	EBSD images, statistics	Εσσε		
Voids	OM images, statistics	$E, \sigma_{ys}, \sigma_{uts}, \varepsilon_{uts}$	Stress-strain curves	
Precipitates	EBSD images, statistics		Stress-strain curves	
Surface roughness	EBSD and OM images, R_a values	$\sigma_{1\%}, \sigma_{2\%}, \sigma_{4\%}, \sigma_{8\%}, \sigma_{16\%}$		

3 Material Modeling Methods

Our overall approach to the challenge was to apply computational crystal plasticity to achieve microstructural sensitivity, solved within either a Fast Fourier

Table 3 Material conditions for calibration and prediction

Testing purpose	Surface treatment	Post build treatment	Build angle	Thickness	Test temperature
Calibration	Ground	SR + HIP + HT / SR	0°	Cylinder	75 °F (23.9 °C) / 1600 °F (871.1 °C)
Prediction	As printed / Ground	SR + HIP + HT / SR	0° / 40°	$1\mathrm{mm}$ / $5\mathrm{mm}$	75 °F (23.9 °C) / 1600 °F (871.1 °C)

Transform-based framework (FFT) or an efficient reduced-order mechanistic computational homogenization scheme, both operating upon a representative volume element (RVE). In both cases, computational crystal plasticity (CP) was used to achieve microstructural sensitivity, allowing our predictions to vary based on the reported crystallographic states.

3.1 Crystal plasticity material model

The computational crystal plasticity material representation used here is identical to that used for the AFRL Challenge 4, described in the companion paper in this Topical Collection [28]. AFRL Challenge 4 requested that participant predict the grain-averaged elastic strain after several different load/strain levels of a polycrystalline tensile test specimen. Thus, our microstructure-based computational method could be applicable to both challenges.

3.2 Fast Fourier Transform-based framework

For our results reported in the competition, we used a FFT-based solution method with CP, termed CPFFT here. The Newton-Krylov solver reported in [29] was implemented, and the surrounding custom framework enabled input of RVEs and the computation of the material response throughout its deformation history, including at each of the requested points. However, because this is an RVE representation, the method is unable to capture localization within the gage section of the tensile coupon. The important implication of this is that ultimate tensile strength (UTS), and strain at UTS, was not predicted or reported for the competion.

3.3 Computational homogenization with self-consistent clustering analysis

The crystal plasticity material model was implemented within Self-consistent Clustering Analysis (SCA) [16], following the method introduced in [30] and refined for finite deformations in [31] and [17]. The data-driven scheme achieves order reduction by discretizing the domain (the RVE, containing a collection of grains in this case) on the basis of similar mechanical response rather than similar location in physical spaces as would be done in, e.g., the finite element

method. Similarity of mechanical response is estimated based upon an initial, preliminary analysis often conducted with a simple material model, and termed the *training* dataset. The training dataset is used by a clustering algorithm to group material points into *clusters*. These groups are then used to assess mechanical response by solving a discrete Lippmann-Schwinger equation, Eq. 1 as shown in [17], which has been shown to be equivalent to solving the stress equation for an RVE with periodic boundary conditions and an remote applied deformation.

$$\mathbf{F}(\mathbf{X}) + \mathbf{\Gamma}^0 * (\mathbf{P}(\mathbf{X}) - \mathbf{C}^0 : \mathbf{F}(\mathbf{X})) - \mathbf{F}^0 = \mathbf{0}, \forall \mathbf{X} \in \mathbf{\Omega},$$
(1)

where $\mathbf{F}(\mathbf{X})$ is the deformation gradient at material point \mathbf{X} , \mathbf{P} is the first Piola-Kirchhoff stress (PK1), \mathbf{C}^0 is an reference stiffness tensor, \mathbf{F}^0 is a far-field loading that in theory could be treated as either deformation- or load-based given proper treatment, $\mathbf{\Omega}$ is the domain of the RVE, and * represents the convolution operator. The term $\mathbf{\Gamma}^0$ is the 4th order Green's operator given by

$$\mathbf{\Gamma}^{0} * (\mathbf{P} - \mathbf{C}^{0} : \mathbf{F}) = \int_{\mathbf{\Omega}} \mathbf{\Gamma}^{0} (\mathbf{X} - \mathbf{X}') : (\mathbf{P} (\mathbf{X}') - \mathbf{C}^{0} : \mathbf{F} (\mathbf{X}')) d\mathbf{\Omega} (\mathbf{X}').$$
(2)

as defined in [17]. As described above, the domain is discretized to enable numerical solution, which mathematically can be described using characteristic functions. In so doing, a cluster-based Lippmann-Schwinger equation can be constructed such that the interaction between each cluster can be isolated an only solved once for a given geometric domain. The discretized equations are solved using a self-consistent iterative scheme. Solution variables within each cluster are assumed to be constant, implying the number of clusters can be thought of as a refinement similar to the number of elements within, e.g., the finite element method.

4 Calibration Methods

4.1 Genetic algorithm

A genetic algorithm was used in optimization method for the calibration of the crystal plasticity parameters. A schematic diagram showing the details of the process is shown in Figure 2. More details of the entire algorithm are explained in the companion paper [28] in the same topical collection. For the calibration, EBSD scan data are used from the data provided by Air Force Research Laboratory. Data from optical microscopy and backscattered electron microscopy were not used. The texture data and grain statistics from the EBSD data were passed to the software package DREAM.3D [32] to generate representative volume element (RVE), which reproduced the grain statistics provided by the AFRL. Different RVEs were generated to represent the statistics for the different conditions under which predictions were requested. For calibration, each RVE has a dimension of $10 \, \text{voxels} \times 10 \, \text{voxels} \times 10 \, \text{voxels}$. Each of the voxel

represents one grain. Therefore, each calibration RVE has 1000 grains. In this modeling approach, we did not consider the damage of the material. Because of the nature of the material model, to multiple calibrations were conducted for the system. Appendix B contains tables of calibrated parameters for the different conditions. Two representative results (one at elevated temperature and one at room temperature) are shown in Figs. 3 and 4. For the room temperature case different parameter sets were calibrated for the 4%, 8%, and 16% strain calculations. The figure shows the prediction result for the 4% strain case.

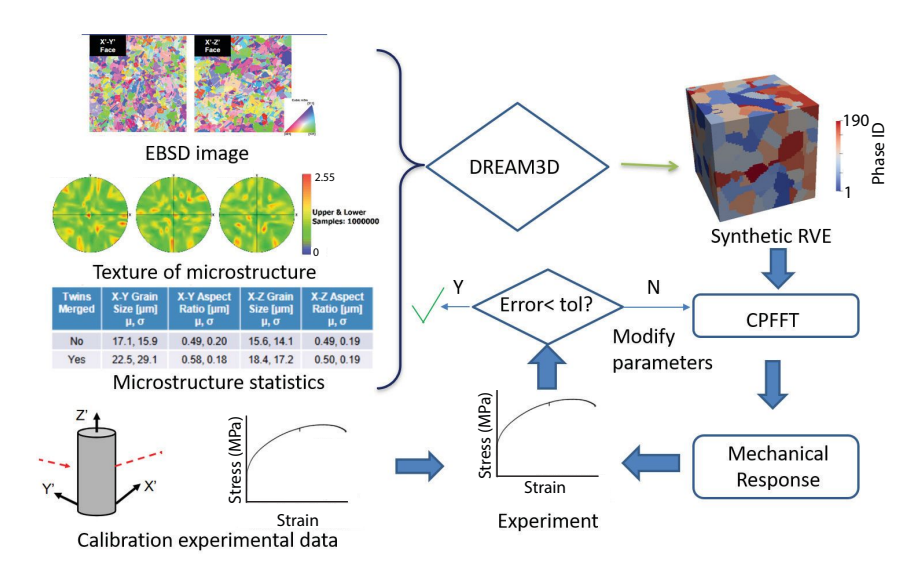


Fig. 2 A schematic diagram showing the steps of the calibration method. CPFFT means crystal plasticity fast Fourier transformation.

4.2 Proper Generalized Decomposition based material identification

As described earlier, optimization with a genetic algorithm is computationally demanding, due to the repetitive running of CPFFT simulations and global optimization. During the post-competition stage, a PGD-based reduced order model [24,25] was used to replace the iterative CPFFT calculations. This work demonstrates the capability by calibrating one of the suggested calibration condition (SP+HIP+HT at room temperature).

In this work, the parametric stress-strain curve is required for materials identification. More specifically, we want a surrogate model relating the parameters and the stress-strain curve. The PGD surrogate model can be written

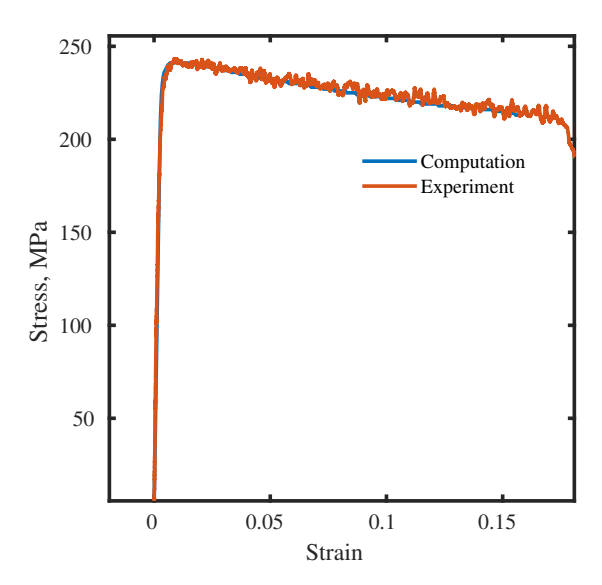


Fig. 3 Calibration results for SR and elevated temperature case.

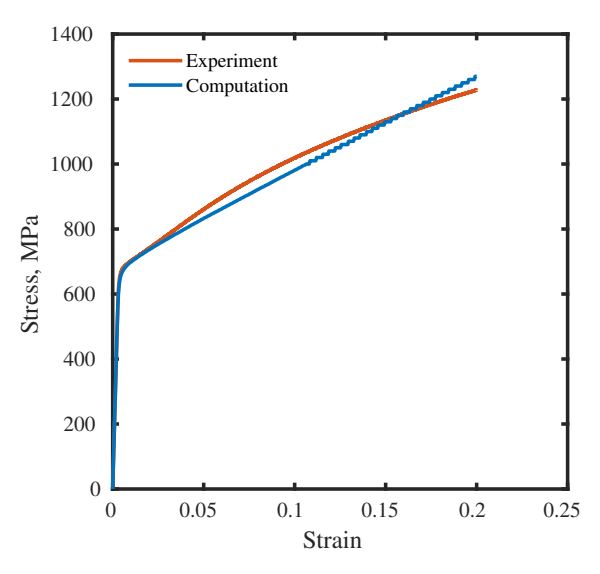


Fig. 4 Calibration results for SR and room temperature case.

as

$$\sigma^{PGD} = \sigma^n(\epsilon, p_1, ..., p_d) = \sum_{m=1}^n F_{\epsilon}^m(\epsilon) F_1^m(p_1) \cdots F_d^m(p_d)$$
 (3)

where p_i are the parameters we want to identify for the crystal plasticity model. n is the rank of the PGD approximation, m denotes the $m^{\rm th}$ mode. Note that the superscripts n, m are counting indicies, not exponentiation. The PGD method [24,25] allows to compute (learn) the unknown functions F^m from given simulation data. Once the training is finished, we obtain the surrogate model relating the parameters and the stress-strain curve. We can then easily vary the values of those p_i and find the best set for a given experimental measure, instead of repetitively running the expensive FFT simulation. Examples of codes can be found on the GitHub project (https://yelugit.github.io/hopgd/).

Now, we can formulate the calibration problem as follows. Assuming the parameters $\boldsymbol{p} = [p_1, \dots, p_d]$ belong to a predefined domain $\mathcal{D} = \mathcal{D}_1 \times \dots \times \mathcal{D}_d$, we want to identify the best \boldsymbol{p}^* such that

$$\boldsymbol{p}^* = \underset{\boldsymbol{p} \in \mathcal{D}}{\operatorname{arg min}} \ J\left(\sigma^{PGD}, \sigma^e, \boldsymbol{p}\right)$$
 (4)

where J denotes the objective function which measures the distance between the model output σ^{PGD} and the experimental measurement σ^e . This calibration problem can be done by any gradient-based optimization algorithm at a very low cost.

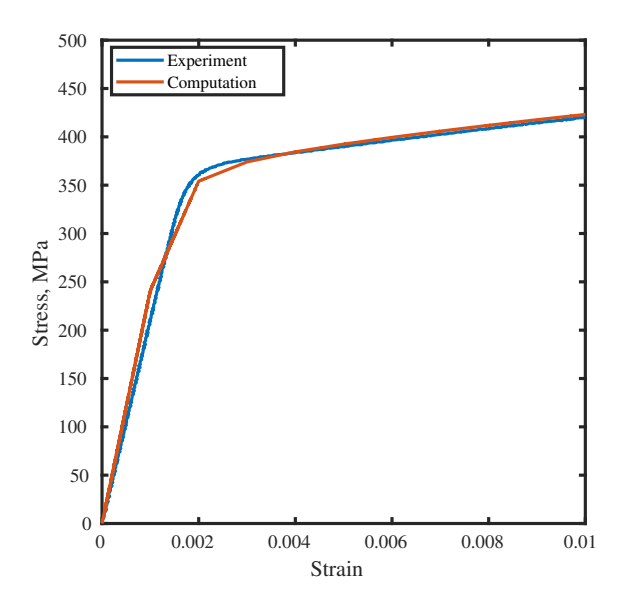
The PGD method is also briefly described in the companion paper for AFRL Challenge 4 [28]. It has been shown that this approach can significantly speed up the calibration. For both the genetic algorithm and PGD-based calibration, 36 2.3 GHz Xeon Gold 6140 processors were used with 192 GB of memory. For the genetic algorithm, the calibration took 3.6 h. Compared to that, the calibration (with calibration data) with PGD took 0.7 h with a speed up by a factor of almost 5. Figure 5 shows the result of the PGD calibration.

5 Challenge Response Analysis

This section will provide a discussion on the challenge response and how SCA can be applied to solve the same set of problems.

5.1 Assumptions and Interpretations

- It is assumed that the average response of the representative volume elements (RVE) is the same as the response of the part.
- EBSD data was given from two locations of the calibration cylinder: middle
 and edge. In order to solve the problems for surface ground specimens the
 RVEs are prepared only from scans from middle EBSD data, and for not
 surface ground specimens only the corner EBSD statistics were considered.
- The voids inside the material are ignored due to low volume fraction (exact amount varied from case to case).



 $\textbf{Fig. 5} \ \ \text{Calibration outcome for optimization using the PGD method with calibration data from AFRL}$

- It is assumed that the effect of temperature can be captured by only calibration of material model parameters.
- The group only reported ultimate tensile strength for the cases of elevated temperature.

5.2 Representative Volume Elements

To address the challenge problems, RVEs for each prediction case were prepared from the EBSD data provided by the AFRL, as mentioned in section 4.1. For the reported predictions, RVEs with dimension of $60 \text{ voxels} \times 60 \text{ voxels} \times 60 \text{ voxels}$ were generated with voxel edge length of 2 µm. The different conditions for which predictions were made had different grain statistics (most importantly mean grain size), thus the number of grains in the respective RVEs were different, varying between 101 and 181. Sampling variability also contributed somewhat to the different instantiations of RVEs having slightly different numbers of grains. To select the RVE size, multiple RVEs of gradually increasing size are generated until the homogenized response converges for subsequently larger RVEs; the size we selected shows consistent results with larger RVEs.

5.3 Responses

For this challenge, the AFRL have not yet released the experimental data for the participants. Hence, the following results will be shown in terms of only the relative accuracy of the prediction based on the points earned. Points earned is a relative measure, where points are correlated to prediction accuracy following the table provided in Appendix A. The results are presented as bar charts showing percentage of available points earned for each prediction in Figs. 6 and 7. The results are in four major groups: surface ground, not surface ground, room temperature, and elevated temperature. Points for other categories are combined into these major groups. Since the methods used were unable to predict ultimate tensile stress and elongation, and thus those results were not reported during the competition, these figures do not consider them for comparison.

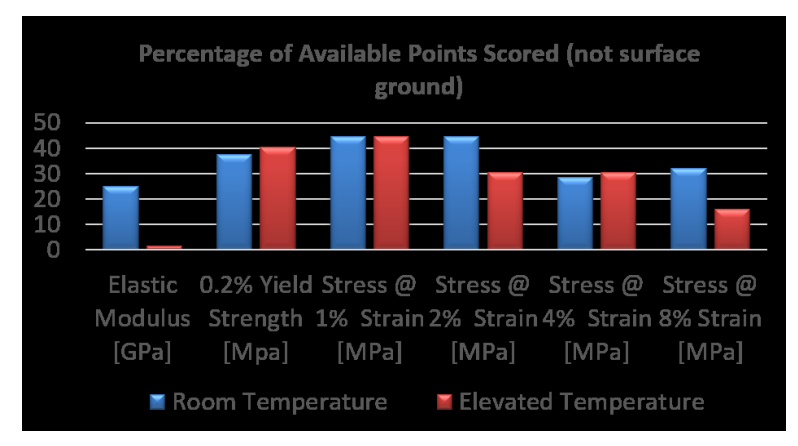


Fig. 6 A bar chart showing the percentage of available points scored for not surface ground conditions. Here, both SR only and SR+HIP+HT conditions, both build angle, and both thickness measured are combined together to count the points. This was done using genetic algorithm.

Figure 6 shows the percentage of available points scored for the not surface ground condition for cases including room temperature and elevated temperature. From the figure it is apparent that our prediction did not do well in predicting the elastic modulus. The reason can be attributed to ignoring the precipitates and voids that were present in the material. These foreign phases ereate strain concentration inside the matrix material thereby increasing the elastic modulus. One reason might be the RVE approximation. The RVEs are generated using the texture information obtained from experiments. It is a statistical inference, and consequently mismatch in the trend is a possibility. However, since there was no experimental data provided, the authors are unable to confidently further investigate the reason. The mismatch could also be because our elastic constants were not fit to experimental data, but taken directly from the reference literature. The predictions are comparatively better for yield strength, stresses at 1 %, 2 %, and 4 % strains. In addition, prediction for elevated temperature properties are better for the plastic regime. Figure 7 presents the similar cases of prediction for surface ground condition. For the

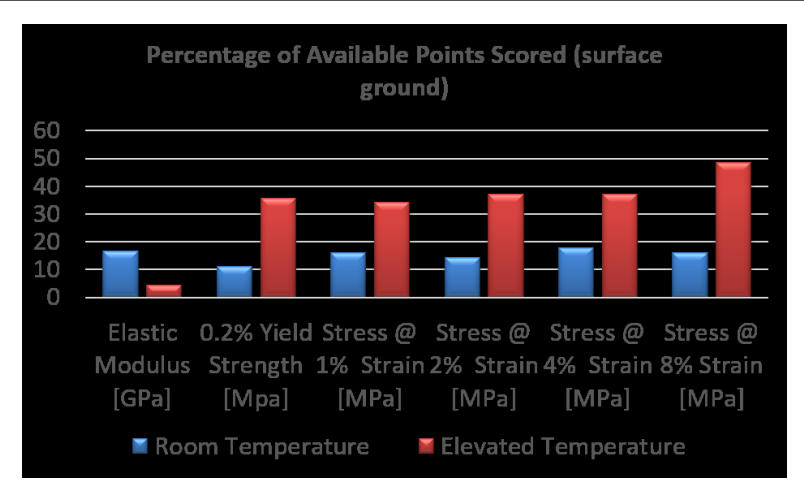


Fig. 7 A bar chart showing the percentage of available points scored for surface ground conditions. Here, both SR only and SR+HIP+HT conditions, both build angle, and both thickness measured are combined together to count the points. This was done using genetic algorithm.

surface ground condition, the elevated temperature predictions are comparatively better.

Figure 8 shows the mechanical response of IN625 samples under different physical conditions. Fig. 8(a) shows that for the 40° angle build, the part becomes relatively stronger. This may be because of the impact of the build angle on the microstructure or grain formation, i.e. the relative change in texture with respect to the load axis. Figure 8(b) implies that surface ground or machined samples are stronger compared to not surface ground condition. This is reasonable since if the surface is ground, the irregular shaped grains are smoothed and there is less chance of failure initiation due to stress concentration at irregular surfaces or grains. However, it is possible for variations to come from the RVE approximation as well. Since the texture is matched statistically to generate the RVE, it is difficult to represent the effect of surface irregularities in the present implementation. Thus, in the RVE, the average grain size may become bigger compared to actual experiment meaning fewer stress concentration and higher strength (our model does not contain a Hall-Petch effect term). Figure 8(c) shows that samples with 5 mm thickness perform better marginally in terms of strength compared to 1 mm thickness samples. Finally, Fig. 8(d) confirms that elevating the temperature will deteriorate the mechanical response in our prediction. However, these are just the prediction values and there is no experimental data released yet to compare against.

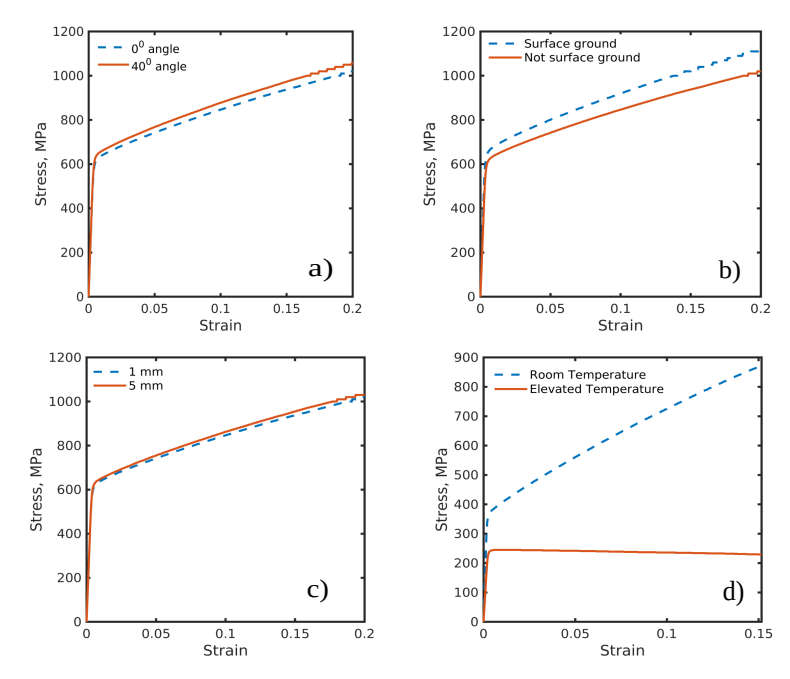


Fig. 8 Predicted mechanical response for different conditions. a) Effect of build angles for specimen at room temperature, SR only, not surface ground, and 1 mm thickness, b) Effect of machining for specimen at room temperature, SR only, 0° build angle, and 1 mm thickness, c) Effect of thickness for specimen at room temperature, SR only, 0° build angle, and not surface ground condition, d) Effect of temperature for specimen with SR+HIP+HT, 0° build angle, 1 mm thickness, and not surface ground condition.

6 Future Outlook

To consider the microstructural features when predicting the part-scale properties it requires a fast computational method. While FFT method used in this work is comparatively faster than FEM, there is still room for improvement. For multiscale computation, where each material point at the macroscale is associated with a smaller scale computation, for instance an RVE, it is expensive to use full-field computation at both scales (or all scales, if more than two are required). The SCA technique can be used to overcome this computational expense, as has been shown in recent work, where the interested reader can find more detailed descriptions [17,18,33]. More detailed information on the technique is given in [17]. The SCA method could also be used to solve the RVE problems for which FFT is applied in for these challenge predictions. In SCA method, the material points are grouped together by clustering those on the basis of elastic strain concentration. The material response is then only computed for each of those clusters, rather than for each material point, by solving a discretized Lippmann-Schwinger equation. As a result, the computation becomes significantly less expensive because the full field solution is

avoided at each material point and solved for each cluster instead. For example, Figure 9a) shows the grains in a demonstrative RVE, and Figure 9b) shows the grouping of material points with two clusters per grain.

A preliminary result, with computations performed with SCA, is shown in Fig. 10 for 1 mm thick, 0° build angle, and SR+HIP+HT sample. The same material parameters are used for both FFT and SCA. Ongoing work will refine the SCA predictions for this case; in theory, the. As can be seen SCA solution converges to the FFT results with a sufficiently large number of clusters [17]. SCA is an attractive proposition since it is a mechanistic reduced order model and can be extended to a multi-scale simulation paradigm [17,18]. However, further verification and validation of the implementation is required.

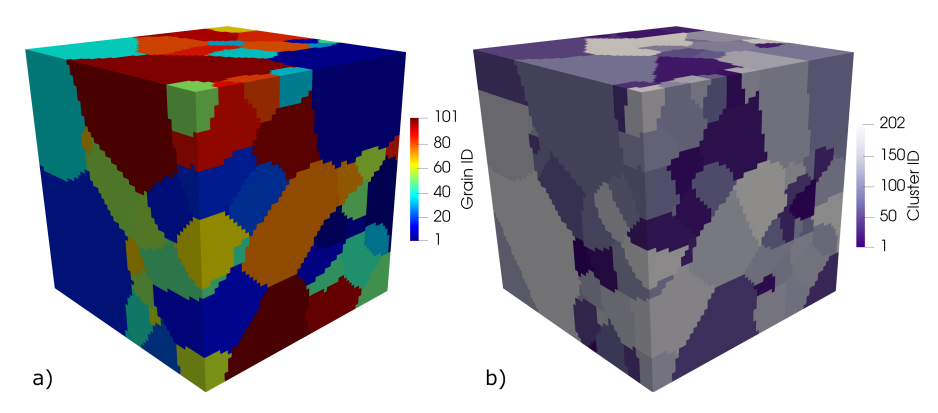


Fig. 9 a) Example microstructure RVE colored by a randomized grain identification number; b) the same RVE, with two clusters per grain, colored by a randomized cluster identification number. This shows the geometric decomposition of microstructure into clusters, for example the large dark blue grain in the top right corner of a) is split vertically in the middle to form two clusters in b).

7 Conclusions

In this article, blind predictions of the quantities requested by the AFRL Challenge 3 are presented. The key takeaway from the challenge include that in order to predict microstructure dependent mechanical properties of material, multiscale and homogenization-based methods are applicable with proper assumptions. The computational cost of calibrating expensive material models can be avoided by using the PGD-based reduced order method. Both full field FFT and reduced-order SCA were shown to be capable of solving these type of problems, and further work will continue to optimize the application of SCA to these types of problems.

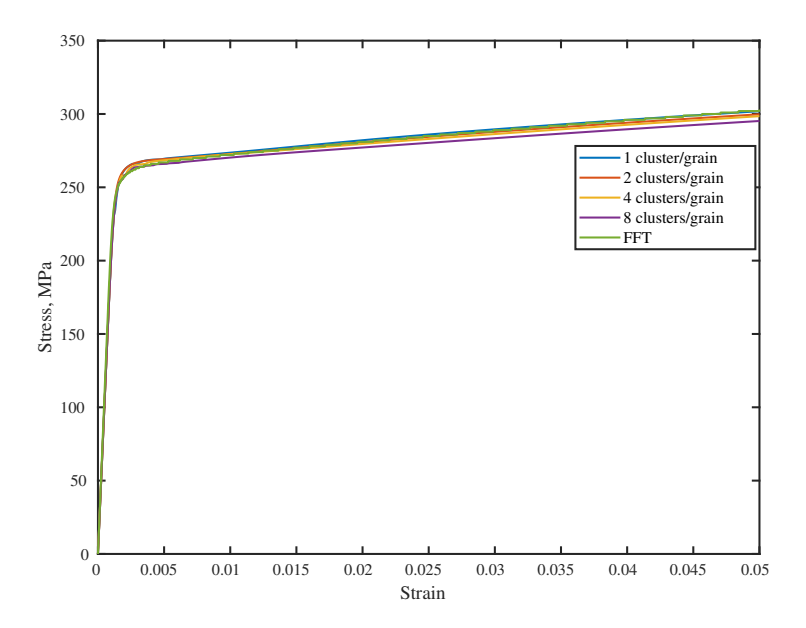


Fig. 10 A comparison of performance for mechanical properties prediction for FFT and SCA with one cluster per grain and two clusters per grain for the 1 mm thick, 0° build angle, and SR+HIP+HT case.

8 Acknowledgements

The authors would like to acknowledge the support of National Science Foundation (NSF, USA) grants CMMI-1762035 and CMMI-1934367; and award no. 70NANB19H005 from U.S. Department of Commerce, National Institute of Standards and Technology as part of the Center for Hierarchical Materials Design (CHiMaD), United States. This research was completed while Orion Kafka held a National Research Council Postdoctoral Research Associateship at the National Institute of Standards and Technology.

Conflict of interest

The authors declare that they have no conflict of interest.

Appendix A AFRL Modeling Series Challenge 3 Scoring Rubric

The AFRL provided an example scoring rubric in the PDF available at time of publication at [26]. This is reproduced in Tab. 4.

For Elastic Modulus (E)	$\pm 3 \text{GPa} = 9 \text{Pts}$
	$\pm 6 \text{GPa} = 3 \text{Pts}$
	$\pm 15 \mathrm{GPa} = 1 \mathrm{Pts}$
For 0.2% Yelid Stress (σ_{YS})	$\pm 10 \mathrm{MPa} = 9 \mathrm{Pts}$
	$\pm 20 \mathrm{MPa} = 3 \mathrm{Pts}$
	$\pm 40 \mathrm{MPa} = 1 \mathrm{Pts}$
For stress at each fixed strain (x5)	$\pm 10 \mathrm{MPa} = 7 \mathrm{Pts}$
	$\pm 20 \mathrm{MPa} = 3 \mathrm{Pts}$
	$\pm 40 \mathrm{MPa} = 1 \mathrm{Pts}$
For Ultimate Tensile Stress (σ_{UTS})	$\pm 10 \mathrm{MPa} = 5 \mathrm{Pts}$
	$\pm 20 \mathrm{MPa} = 2 \mathrm{Pts}$
	$\pm 40 \mathrm{MPa} = 1 \mathrm{Pts}$
For Uniform Elongation (ε_{UTS})	$\pm 0.02 = 3 \text{Pts}$
	$\pm 0.04 = 2 \mathrm{Pts}$
	$\pm 0.08 = 1 \mathrm{Pts}$

Table 4 Preliminary scoring rubric, as provided by the AFRL Challenge website [26] at time of publication.

Appendix B Calibrated Parameters

Table 5 A summary of calibrated parameters from optimization using the genetic algorithm and proper generalized decomposition (PGD).

Material Properties	SR, RT**	SR,ET***	SR+HIP+HT,RT	SR+HIP+HT,ET
C1111*	243 300 MPa	94887 MPa	243 300 MPa	133 815 MPa
C1122*	$156700\mathrm{MPa}$	61 113 MPa	$156700{ m MPa}$	$86185\mathrm{MPa}$
C2323*	$117800\mathrm{MPa}$	$45942\mathrm{MPa}$	$117800\mathrm{MPa}$	64790 MPa
$\dot{\gamma}_0$	0.00242	0.00242	0.00242	0.00242
m	58.8	58.8	58.8	58.8
τ_0	$252 \mathrm{MPa}$	101.02 MPa	$140\mathrm{MPa}$	$109.4\mathrm{MPa}$
a	0.025	0.0	0.005	0.0
H	1.0	1.0	1.0	1.0
h	1.5	1.5	4.8985	2.7
R	480.8689	88.8689	601.5983	124.8689
r	1.9425	1.9425	14.0267	1.9425

^{*} From [34]

References

- Wentao Yan, Yanping Lian, Cheng Yu, Orion L Kafka, Zeliang Liu, Wing Kam Liu, and Gregory J Wagner. An integrated process-structure-property modeling framework for additive manufacturing. Computer Methods in Applied Mechanics and Engineering, 339:184-204, 2018.
- 2. M M Francois, A Sun, W E King, N J Henson, D Tourret, C A Bronkhorst, N N Carlson, C K Newman, T Haut, J Bakosi, J W Gibbs, V Livescu, S A Vander Wiel, A J Clarke, M W Schraad, T Blacker, H Lim, T Rodgers, S Owen, F Abdeljawad, J Madison, A T Anderson, J-L. Fattebert, R M Ferencz, N E Hodge, S A Khairallah, and O Walton. Modeling of additive manufacturing processes for metals: Challenges and opportunities. Current Opinion in Solid State and Materials Science, 21(4):198–206, 2017.
- 3. William J Sames, FA List, Sreekanth Pannala, Ryan R Dehoff, and Sudarsanam Suresh Babu. The metallurgy and processing science of metal additive manufacturing. *International Materials Reviews*, 61(5):315–360, 2016.

- 4. Jacob Smith, Wei Xiong, Wentao Yan, Stephen Lin, Puikei Cheng, Orion L Kafka, Gregory J Wagner, Jian Cao, and Wing Kam Liu. Linking process, structure, property, and performance for metal-based additive manufacturing: computational approaches with experimental support. Computational Mechanics, 57(4):583–610, 2016.
- Saeede Ghorbanpour, Milovan Zecevic, Anil Kumar, Mohammad Jahedi, Jonathan Bicknell, Luke Jorgensen, Irene J Beyerlein, and Marko Knezevic. A crystal plasticity model incorporating the effects of precipitates in superalloys: application to tensile, compressive, and cyclic deformation of Inconel 718. International Journal of Plasticity, 99:162

 185, 2017
- 6. Veerappan Prithivirajan and Michael D Sangid. The role of defects and critical pore size analysis in the fatigue response of additively manufactured IN718 via crystal plasticity. *Materials & Design*, 150:139–153, 2018.
- Ali Tabei, Elham Mirkoohi, Hamid Garmestani, and Steven Liang. Modeling of texture development in additive manufacturing of Ni-based superalloys. The International Journal of Advanced Manufacturing Technology, 103(1):1057–1066, 2019.
- HL Wei, T Mukherjee, W Zhang, JS Zuback, GL Knapp, A De, and T DebRoy. Mechanistic models for additive manufacturing of metallic components. *Progress in Materials Science*, page 100703, 2020.
- 9. H Moulinec and P Suquet. A numerical method for computing the overall response of nonlinear composites with complex microstructure. Computer Methods in Applied Mechanics and Engineering, 157(1-2):69–94, 1998.
- 10. Ted Belytschko, Wing Kam Liu, Brian Moran, and Khalil Elkhodary. *Nonlinear finite elements for continua and structures*. John Wiley & Sons, 2013.
- Ricardo A Lebensohn, Anand K Kanjarla, and Philip Eisenlohr. An elasto-viscoplastic formulation based on fast fourier transforms for the prediction of micromechanical fields in polycrystalline materials. *International Journal of Plasticity*, 32:59–69, 2012.
- 12. Theron M. Rodgers, Joseph E. Bishop, and Jonathan D. Madison. Direct numerical simulation of mechanical response in synthetic additively manufactured microstructures. *Modelling and Simulation in Materials Science and Engineering*, 26(5), 2018.
- 13. Frédéric Feyel and Jean-Louis Chaboche. FE2 multiscale approach for modelling the elastoviscoplastic behaviour of long fibre SiC/Ti composite materials. Computer Methods in Applied Mechanics and Engineering, 183(3-4):309–330, 2000.
- 14. Julian Kochmann, Stephan Wulfinghoff, Stefanie Reese, Jaber Rezaei Mianroodi, and Bob Svendsen. Two-scale FE-FFT- and phase-field-based computational modeling of bulk microstructural evolution and macroscopic material behavior. *Computer Methods in Applied Mechanics and Engineering*, 305:89–110, 2016.
- Karel Matouš, Marc GD Geers, Varvara G Kouznetsova, and Andrew Gillman. A review of predictive nonlinear theories for multiscale modeling of heterogeneous materials. *Journal of Computational Physics*, 330:192–220, 2017.
- Zeliang Liu, M. A. Bessa, and Wing Kam Liu. Self-consistent clustering analysis: An
 efficient multi-scale scheme for inelastic heterogeneous materials. Computer Methods in
 Applied Mechanics and Engineering, 306:319–341, 2016.
- Cheng Yu, Orion L Kafka, and Wing Kam Liu. Self-consistent clustering analysis for multiscale modeling at finite strains. Computer Methods in Applied Mechanics and Engineering, 349:339–359, 2019.
- 18. Orion L. Kafka, Kevontrez K. Jones, Cheng Yu, Puikei Cheng, and Wing Kam Liu. Image-based multiscale modeling with spatially varying microstructures from experiments: Demonstration with additively manufactured metal in fatigue and fracture. Journal of the Mechanics and Physics of Solids, page 104350, 2021.
- Orion L Kafka, Cheng Yu, Modesar Shakoor, Zeliang Liu, Gregory J Wagner, and Wing Kam Liu. Data-driven mechanistic modeling of influence of microstructure on high-cycle fatigue life of nickel titanium. JOM, 70(7):1154–1158, 2018.
- 20. Peter Bate. Modelling deformation microstructure with the crystal plasticity finite-element method. Philosophical Transactions of the Royal Society of London. Series A: Mathematical, Physical and Engineering Sciences, 357(1756):1589–1601, 1999.
- 21. Franz Roters, Philip Eisenlohr, Luc Hantcherli, Denny Dharmawan Tjahjanto, Thomas R Bieler, and Dierk Raabe. Overview of constitutive laws, kinematics, homogenization and multiscale methods in crystal plasticity finite-element modeling: Theory, experiments, applications. Acta Materialia, 58(4):1152–1211, 2010.

22. Kartik Kapoor, Priya Ravi, Ryan Noraas, Jun-Sang Park, Vasisht Venkatesh, and Michael D Sangid. Modeling Ti–6Al–4V using crystal plasticity, calibrated with multiscale experiments, to understand the effect of the orientation and morphology of the α and β phases on time dependent cyclic loading. *Journal of the Mechanics and Physics of Solids*, 146:104192, 2021.

- 23. Dhyanjyoti Deka, Deepu S Joseph, Somnath Ghosh, and Michael J Mills. Crystal plasticity modeling of deformation and creep in polycrystalline Ti-6242. *Metallurgical and Materials Transactions A*, 37(5):1371–1388, 2006.
- 24. Y Lu, N Blal, and A Gravouil. Adaptive sparse grid based HOPGD: Toward a nonintrusive strategy for constructing space-time welding computational vademecum. International Journal for Numerical Methods in Engineering, 114(13):1438–1461, 2018.
- Y Lu, N Blal, and A Gravouil. Datadriven HOPGD based computational vademecum for welding parameter identification. Computational Mechanics, 64(1):47–62, 2019.
- Air Force Research Laboratory (AFRL) Additive Manufacturing (AM) Modeling Challenge Series. https://materials-data-facility.github.io/MID3AS-AM-Challenge/, February 2021. [Accessed: 4 March 2021].
- ASTM E8 / E8M-16ae1. Standard Test Methods for Tension Testing of Metallic Materials. 2021.
- Sourav Saha, Orion L. Kafka, Ye Lu, Cheng Yu, and Wing Kam Liu. Microscale structure to property prediction for additively manufactured IN625 through advanced material model parameter identification. *Integrating Materials and Manufacturing Innovation (submitted)*, 2021.
- Matthias Kabel, Thomas Böhlke, and Matti Schneider. Efficient fixed point and Newton-Krylov solvers for FFT-based homogenization of elasticity at large deformations. Computational Mechanics, 54(6):1497–1514, 2014.
- Zeliang Liu, Orion L Kafka, Cheng Yu, and Wing Kam Liu. Data-driven self-consistent clustering analysis of heterogeneous materials with crystal plasticity. In *Advances in Computational Plasticity*, pages 221–242. Springer, 2018.
- 31. Modesar Shakoor, Orion L. Kafka, Cheng Yu, and Wing Kam Liu. Data science for finite strain mechanical science of ductile materials. *Computational Mechanics*, 64(1):33–45, 2018
- 32. Michael A Groeber and Michael A Jackson. Dream. 3d: a digital representation environment for the analysis of microstructure in 3d. *Integrating materials and manufacturing innovation*, 3(1):56–72, 2014.
- Cheng Yu, Orion L. Kafka, and Wing Kam Liu. Multiresolution clustering analysis for efficient modeling of hierarchical material systems. *Computational Mechanics*, 67(5):1293–1306, May 2021.
- 34. Zhuqing Wang, Alexandru D. Stoica, Dong Ma, and Allison M. Beese. Diffraction and single-crystal elastic constants of Inconel 625 at room and elevated temperatures determined by neutron diffraction. *Materials Science and Engineering: A*, 674:406–412, 2016.